ARTICLE OPEN

Check for updates

Csnk1a1 E98 mutations rewire signaling and metabolism in del(5q) myelodysplastic neoplasms

Stephani Schmitz[1,2,16], Juliette E. Pearce[3,16], Sergio Martinez-Høyer[1,2,4], Gerjanne Vroeg in de wei[1,2], Inge A. M. Snoeren[1,2], Ursula S. A. Stalmann[1,2], Stijn N. R. Fuchs[1,2], Aurelien J. F. Dugourd[5], Giulia Franciosa[6], Eric M. Bindels[7], Wencke Walter[8], Claudia Meyer[9], Torsten Haferlach[8], Emiel P. C. van der Vorst[10,11], Oriol Calvete[12], Francesc Solé[12], Julio Saez-Rodriguez[5,13], Andreas Linkermann[9,14,15], Jesper Olsen[6], Hélène F. E. Gleitz[1,2] and Rebekka K. Schneider[1,2,3]✉

© The Author(s) 2026

Deletion of chromosome 5q [del(5q)] is the most common cytogenetic abnormality in myelodysplastic neoplasms (MDS) and results in haploinsufficiency of multiple genes, including *CSNK1A1*. Recurrent *CSNK1A1* mutations, predominantly affecting the E98 hotspot, occur almost exclusively in del(5q) MDS and are associated with adverse outcomes, yet their impact on CK1α function remains unclear. Using integrated transcriptomic, (phospho)proteomic, and kinome activity profiling in hematopoietic stem and progenitor cells (HSPCs), combined with in vivo serial transplantation assays, we show that *Csnk1a1* E98V represents a change-of-function rather than a loss-of-function mutation. Unlike *Csnk1a1* haploinsufficiency, *Csnk1a1* E98V preserves long-term hematopoietic reconstitution and does not enhance clonal expansion in vivo. Instead, the mutation induces suppression of kinase signaling networks, leading to coordinated repression of ribosomal gene expression, protein translation, and cell cycle programs. This signaling rewiring is accompanied by metabolic reprogramming characterized by reduced mitochondrial respiration, increased glycolytic flux, and an inability to adapt to metabolic challenges, creating a stress-tolerant but inflexible cellular state. Notably, *Csnk1a1* E98V cells exhibit impaired megakaryopoiesis and increased vulnerability to iron overload, as well as RSL-3-mediated ferroptosis. Analysis of del(5q) MDS patients confirmed that *CSNK1A1* mutations are associated with distinct clinical features, including thrombocytopenia, elevated myeloblasts, and reduced bone marrow iron levels. Together, our findings support a two-step model in which del(5q)-associated *CSNK1A1* haploinsufficiency drives clonal expansion, followed by acquisition of *CSNK1A1* mutations that promote stress tolerance rather than increased proliferation. This adaptive rewiring exposes metabolic and iron-dependent vulnerabilities that may be therapeutically exploited.

Leukemia; https://doi.org/10.1038/s41375-026-03122-x

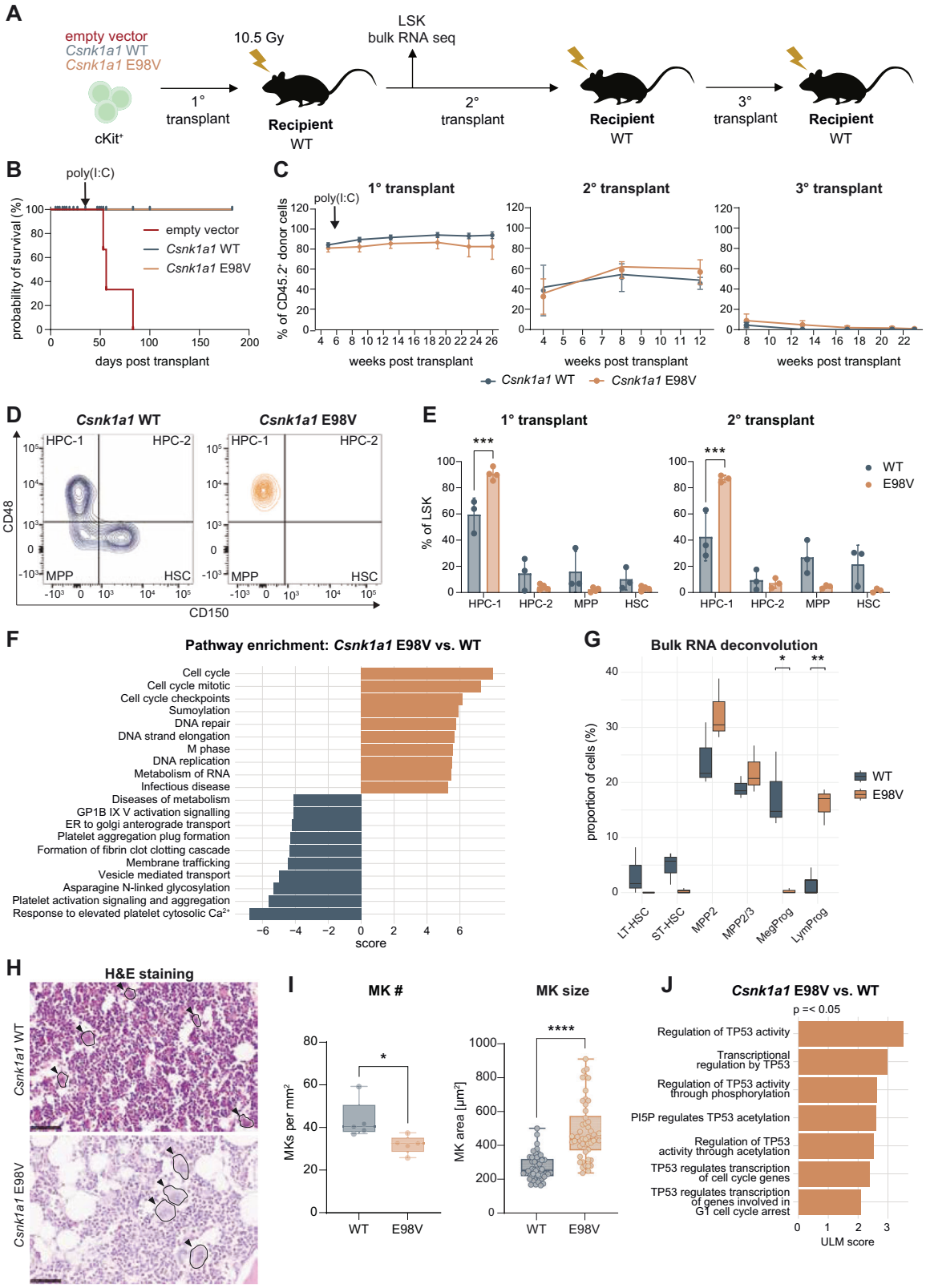
INTRODUCTION

Myelodysplastic neoplasms (MDS) are a heterogeneous group of clonal hematologic disorders characterized by ineffective hematopoiesis, cytopenias, and an increased risk of progression to acute myeloid leukemia (AML) [1, 2]. The most frequent cytogenetic abnormality represented in 10–15% of MDS cases is an interstitial deletion in the long arm of chromosome 5 [del(5q)] [3, 4], which arises in hematopoietic stem cells (HSCs) and confers a selective growth advantage. Del(5q) results in haploinsufficiency of a number of genes, including *CSNK1A1* [encoding casein kinase 1α1 (CK1α)], a serine/threonine kinase that regulates many crucial pathways, including WNT/β-catenin, p53, and NF-κB signaling [5–7]. In line with this, experimental models have shown that complete loss of *Csnk1a1* leads to bone marrow failure, while haploinsufficiency promotes HSC expansion and self-renewal, highlighting a dosage-sensitive role in hematopoietic homeostasis and clonal fitness [8, 9]. This dosage dependence is reflected in the therapeutic mechanism of lenalidomide, which induces proteasomal degradation of CK1α, thereby selectively eliminating del(5q) clones [10].

Beyond the *CSNK1A1* haploinsufficiency caused by del(5q), approximately 10–15% of del(5q) MDS patients acquire somatic mutations in the remaining *CSNK1A1* allele, most frequently affecting the residue E98 [8, 11–13]. These secondary mutations

[1]Department of Developmental Biology, Erasmus Medical Center, Rotterdam, The Netherlands. [2]Oncode Institute, Erasmus Medical Center Cancer Institute, Rotterdam, The Netherlands. [3]Department of Cell and Tumor Biology, Faculty of Medicine, Rheinisch-Westfälische Technische Hochschule Aachen University, Aachen, Germany. [4]Microbiology, Tumor and Cell Biology, Karolinska Institute, Stockholm, Sweden. [5]Heidelberg University, Faculty of Medicine, and Heidelberg University Hospital, Institute for Computational Biomedicine, Heidelberg, Germany. [6]Novo Nordisk Foundation Center for Protein Research, Copenhagen, Denmark. [7]Department of Hematology, Erasmus Medical Center Cancer Institute, Rotterdam, The Netherlands. [8]MLL Munich Leukemia Laboratory, Munich, Germany. [9]Department of Medicine V, University Medical Centre Mannheim, University of Heidelberg, Mannheim, Germany. [10]Department of Internal Medicine I – Cardiology, Uniklinik RWTH Aachen, RWTH Aachen University, Aachen, Germany. [11]Institute for Cardiovascular Prevention (IPEK), Ludwig-Maximilians-Universität, Munich, Germany. [12]MDS Group, Josep Carreras Leukaemia Research Institute (IJC), ICO-Hospital Germans Trias i Pujol, Universitat Autònoma de Barcelona (UAB), Badalona, Spain. [13]European Molecular Biology Laboratory, European Bioinformatics Institute, Hinxton, UK. [14]Department of Internal Medicine 3, University Hospital Carl Gustav Carus at the Technische Universität Dresden, Dresden, Germany. [15]Division of Nephrology, Department of Medicine, Albert Einstein College of Medicine, New York, NY, USA. [16]These authors contributed equally: Stephani Schmitz, Juliette E. Pearce. ✉email: reschneider@ukaachen.de

Received: 24 April 2026 Revised: 23 July 2026 Accepted: 12 August 2026
Published online: 03 September 2026



are associated with worse clinical prognosis and reduced lenalidomide response, higher risk of AML progression, and shorter overall survival [12, 13]. Although previous studies established CSNK1A1 as a dosage-sensitive driver of del(5q) MDS biology, the functional consequences of recurrent hotspot mutations remain poorly understood. In particular, it is unclear whether these mutations simply mimic reduced CK1α dosage or instead confer mutant-specific signaling, metabolic, or clonal properties.

To address this question, we investigated how the *Csnk1a1 E98V* mutation alters CK1α function in hematopoiesis using genetic and

Fig. 1 *Csnk1a1* E98V retains functional activity in vivo but remodels hematopoietic stem and progenitor cell composition. c-Kit-enriched BM cells from *Csnk1a1*$^{fl/fl}$ Mx1-Cre^{+} CD45.2^{+} donor mice were retrovirally transduced with pMIG–based vectors encoding *Csnk1a1* WT, *Csnk1a1* E98V, or empty vector (EV) controls. Transduced cells were transplanted into lethally irradiated CD45.1^{+} WT recipient mice. 40 days post transplantation, endogenous *Csnk1a1* was deleted by intraperitoneal administration of poly(I:C). Mice were analyzed at 26 weeks post-transplant. Whole BM from *Csnk1a1* WT and *Csnk1a1* E98V primary recipients was transplanted into lethally irradiated CD45.1^{+} WT secondary recipients, which were analyzed 12 weeks later. Whole BM from secondary recipients was similarly transplanted into tertiary recipients, which were analyzed 23 weeks post-transplant. **A** Schematic overview of the experimental design. **B** Survival analysis of primary recipient mice following poly(I:C) administration, comparing EV ($n = 3$), *Csnk1a1* WT ($n = 3$), and *Csnk1a1* E98V ($n = 4$). **C** Donor-derived CD45.2^{+} PB chimerism assessed by flow cytometry across primary (left; *Csnk1a1* WT $n = 3$ mice, *Csnk1a1* E98V $n = 4$ mice), secondary (middle; $n = 3$ mice per group) and tertiary (right; $n = 5$ mice per group) transplants. Data represent mean ± SD. **D** Representative flow cytometric gating strategy for identification and analysis of BM-derived lin^{-}Sca-1^{+}c-Kit^{+} (LSK) HSPCs and their downstream subpopulations: CD48^{+}CD150^{-} (HPC-1), CD48^{+}CD150^{+} (HPC-2), CD48^{-}CD150^{-} (MPP), and CD48^{-}CD150^{+} (HSC). **E** Flow cytometric quantification of HSPC subpopulations in BM from primary (left) and secondary (right) recipients. Individual data points represent one mouse. Data represent mean ± SD. Statistical comparisons were performed using 2-way ANOVA with Šidák multiple comparisons test. **F** Reactome pathway enrichment analysis of DEGs from GFP^{+} LSK cells isolated from primary recipients ($n = 3$ mice per group). Top 10 up- and downregulated pathways shown. **G** CIBERSORT-based computational deconvolution of bulk RNA-seq data to estimate the relative fractional contribution of distinct HSPC populations within GFP^{+} LSK samples. Data are shown as box plots (median, IQR, whiskers extend to 1.5 × IQR). Statistical comparisons were performed using unpaired two-tailed t-tests. **H** Representative histological images of H&E-stained tibial BM sections from *Csnk1a1* WT (top) and *Csnk1a1* E98V (bottom) primary recipients at sacrifice, highlighting MK morphology and distribution. Original magnification: ×40; scale bar: 50 µm. **I** Quantification of MK number per mm^2 (left) and MK size in µm^2 (right) in tibial BM sections from *Csnk1a1* WT and *Csnk1a1* E98V mice. Five randomly selected high-power fields were quantified for number, and 50 MKs were measured for size; $n = 3$ mice per group. Data are shown as box plots (median, IQR, min–max). Statistical comparisons were performed using unpaired two-tailed t-tests. **J** Reactome pathway enrichment of P53-associated pathways, based on DEGs from GFP^{+} LSK cells isolated from primary recipients ($n = 3$ mice per group). Pathways with $p \leq 0.05$ are shown. *$p \leq 0.05$; **$p \leq 0.01$; ***$p \leq 0.001$; ****$p \leq 0.0001$. BM, bone marrow; DEGs, differentially expressed genes; EV, empty vector; H&E, hematoxylin and eosin; HSC, hematopoietic stem cells; HSPCs, hematopoietic stem and progenitor cells; HPC-1, hematopoietic progenitor cells-1; HPC-2, hematopoietic progenitor cells-2; LT-HSCs, long-term HSCs; LymProg, lymphoid progenitors; MDS, myelodysplastic syndrome; MegProg, megakaryocyte progenitors; MK, megakaryocyte; MPP, multipotent progenitors; MPP2/3, multipotent progenitors (subsets 2/3); PB, peripheral blood; SD, standard deviation; ST-HSCs, short-term HSCs; WT, wild-type.

functional models combined with in vivo serial transplantation, transcriptomic, proteomic, phosphoproteomic, kinome, and metabolic profiling. Our results show that the *Csnk1a1* E98V mutation rewires CK1α-dependent signaling and alters differentiation programs, suggesting a previously unrecognized mechanism of clonal adaptation in del(5q) MDS. While *Csnk1a1* haploinsufficiency alone drives HSC expansion, the E98V variant does not further enhance this proliferative phenotype but instead redirects kinase signaling toward distinct metabolic programs, resulting in specific vulnerabilities. Analyses of patient cohorts further indicate that CSNK1A1-mutant del(5q) MDS exhibits distinct clinical and hematologic features, supporting a functional impact beyond simple haploinsufficiency. These insights highlight how *CSNK1A1* mutations can alter cellular fitness and may present a novel avenue for complementary therapies to improve outcomes for patients with *CSNK1A1*-mutant del(5q) MDS.

SHORT METHODS

Mouse models and transplantation experiments

Csnk1a1 conditional knockout mice (*Csnk1a1*$^{fl/fl}$ Mx1-Cre^{+}) were generated as previously described [8]. cKit^{+} bone marrow (BM) cells were retrovirally transduced with *CSNK1A1* WT, *CSNK1A1* E98V, or empty vector controls and transplanted into lethally irradiated (10.5 Gy) CD45.1 (B6.SJL) recipient mice. Conditional deletion was induced by poly(I:C) injection (3× at 5 mg/g) 40 days post-transplant. Serial transplantations were performed using 2×10^6 whole BM cells. Peripheral blood was periodically collected from mice via submandibular bleeds. At experiment endpoints, BM cells were isolated by crushing spine, pelvis, femurs, and tibiae, and labeled with directly conjugated anti-mouse antibodies for analysis via flow cytometry.

Cell line generation and functional assays

Primary murine BM cells from *Csnk1a1*$^{fl/fl}$ Mx1-Cre^{+} or *Csnk1a1*$^{fl/+}$ Mx1-Cre^{+} mice were immortalized through retroviral transduction with MSCV-ERHBD-Hoxb8 constructs as previously described [14]. Immortalized cells were transduced with MSCV-IRES-GFP vectors encoding *CSNK1A1* WT or *CSNK1A1* E98V. Endogenous *Csnk1a1* alleles were excised by IFNα treatment, and single GFP^{+} clones were isolated by FACS. Kinome activity profiling was performed using PamChip® STK arrays (PamGene International) with 2.0 µg protein lysate. Additional functional assays are detailed in Supplementary Methods.

Multi-omics profiling

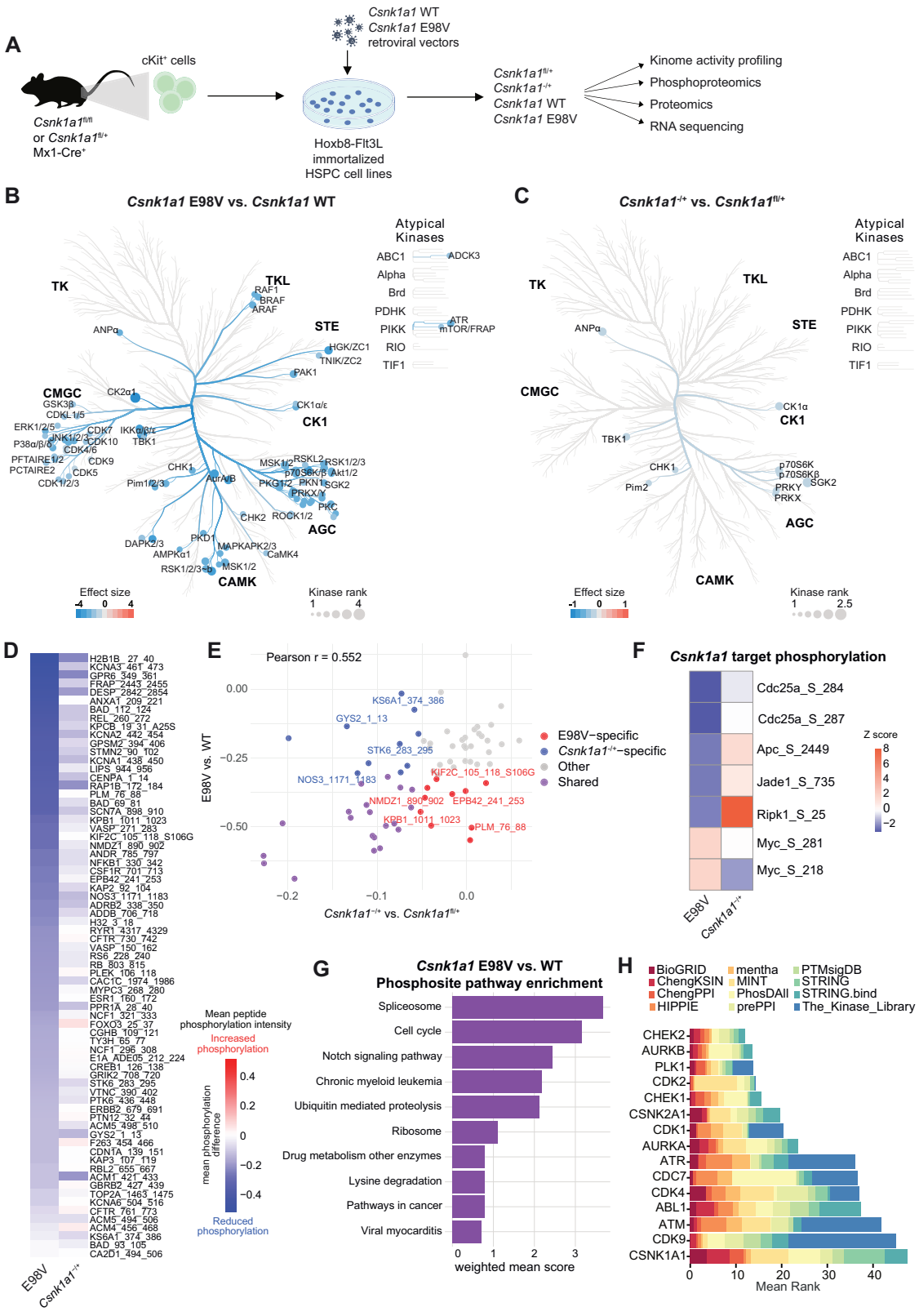
For RNA-sequencing, GFP^{+}Lin^{-}Sca1^{+}c-Kit^{+} cells were sorted from mouse BM into TRIzol-LS, and Hoxb8 cell lines were collected in TRIzol. RNA libraries were prepared using the Smart-Seq V4 Ultra low input RNA kit (Clontech Laboratories) and the KAPA RNA Hyperprep Kit with RiboErase (HMR) (Roche), respectively, and sequenced on an Illumina NovaSeq 6000, generating paired-end reads. Transcript-level quantification was performed using the Salmon pipeline (v1.8.0), and differential expression analysis was performed using limma. For proteomics and phosphoproteomics, Hoxb8 cell line samples were processed for tandem mass tag profiling and quantified using MaxQuant. Differential analysis was performed using the R package limma, and pathway enrichment for both datasets was conducted using decoupleR and clusterProfiler. Processed RNA sequencing and (phospho)proteomics data are available upon request.

Patient cohort

A total of 195 samples were obtained from patients referred for diagnostic evaluation to the Munich Leukemia Laboratory. Of these, 111 patients had isolated del(5q) without *CSNK1A1* mutations, while 84 harbored *CSNK1A1* mutations in addition to del(5q). Routine diagnostic analyses included cytomorphology, conventional chromosome banding analysis, FISH, and targeted molecular genetic analysis. Complete blood counts were performed by the referring physicians. Patient characteristics are detailed in Supplementary Table 1.

Ethics approval and consent to participate

Mouse experiments were performed according to protocols approved by the Central Animal Committee (Centrale Commissie Dierproeven; CCD; The Netherlands under approval numbers no. AVD1010020173387 and no. AVD101020216373). Bone marrow and/or peripheral blood samples were obtained from patients referred for diagnostic evaluation to the Munich Leukemia



Laboratory. All patients gave their written informed consent for genetic analyses and for the use of laboratory results and clinical data for research purposes according to the Declaration of Helsinki. The study was further approved by the laboratory's institutional review board.

RESULTS

Csnk1a1 E98V retains functional activity and supports hematopoiesis in vivo

Previous studies have demonstrated that complete loss of *Csnk1a1* leads to hematopoietic failure, while haploinsufficiency promotes

Fig. 2 The *Csnk1a1* E98V mutation rewires kinase signaling beyond simple loss of function. Conditionally immortalized hematopoietic progenitor cell lines were generated from Mx1-Cre$^+$ *Csnk1a1*$^{fl/fl}$ and Mx1-Cre$^+$ *Csnk1a1*$^{fl/+}$ BM using the Hoxb8-Flt3L system. Endogenous *Csnk1a1* was excised through Cre recombination and WT or E98V-mutant *Csnk1a1* was expressed via retroviral transduction. **A** Schematic overview of the experimental design. Kinome tree visualization of inferred kinase activity from PamChip serine/threonine peptide (STK) microarray comparing *Csnk1a1* E98V ($n = 4$) to *Csnk1a1* WT ($n = 3$) (**B**) and *Csnk1a1*$^{-/+}$ ($n = 4$) to *Csnk1a1*$^{fl/+}$ ($n = 4$) (**C**). Tree branches represent kinase families; color intensity and node size indicate direction and magnitude of inferred activity. **D** Difference in mean peptide phosphorylation intensity (mutant - control) for 71 peptides derived from the STK microarray. Left: *Csnk1a1* E98V vs. *Csnk1a1* WT. Right: *Csnk1a1*$^{-/+}$ vs. *Csnk1a1*$^{fl/+}$. *Csnk1a1* WT $n = 3$, *Csnk1a1* E98V $n = 4$ biological replicates. **E** Scatter plot of peptide-level phosphorylation changes derived from the STK microarray comparing *Csnk1a1* E98V and *Csnk1a1*$^{-/+}$ conditions vs. their respective controls. Each dot represents a phosphopeptide; values correspond to the mean phosphorylation differences between conditions for each peptide. Peptides were ranked separately for each comparison based on the absolute value of these mean phosphorylation differences. The 30 highest-ranked peptides from each comparison were classified as shared (present in both ranked sets), E98V-specific or *Csnk1a1*$^{-/+}$-specific based on overlap between sets. All peptides not included among the top 30 ranked peptides in either comparison are denoted as other. *Csnk1a1* WT n = 3, *Csnk1a1* E98V $n = 4$ biological replicates. **F** Phosphorylation levels of known *Csnk1a1* targets measured by quantitative phosphoproteomics. Individual sites are shown for *Csnk1a1* E98V vs. *Csnk1a1* WT (left) and *Csnk1a1*$^{-/+}$ vs. *Csnk1a1*$^{fl/+}$ (right). $n = 3$ biological replicates per group. **G** Top 10 pathways identified by weighted mean statistical enrichment analysis of differentially phosphorylated sites identified by quantitative phosphoproteomics in *Csnk1a1* E98V vs. *Csnk1a1* WT cells. $n = 3$ biological replicates per group. **H** Kinase enrichment analysis performed using KEA3, showing the top 15 ranked kinases inferred to be upstream of genes identified as containing phosphosites with decreased phosphorylation in *Csnk1a1* E98V compared to *Csnk1a1* WT cells. $n = 3$ biological replicates per group. Color signifies the database used to infer kinases. AGC protein kinase A/G/C, BM bone marrow, CAMK calcium/calmodulin-dependent kinase, CK1 casein kinase 1, CMGC CDK/MAPK/GSK3/CLK kinase family, STK serine/threonine kinase, STE sterile kinase, TK tyrosine kinase, TKL tyrosine kinase-like, WT wild-type.

clonal HSC expansion [8]. However, the functional consequences of recurrent *Csnk1a1* mutations remain unknown. To investigate the effect of the *CSNK1A1* E98V mutation on hematopoiesis, we employed a conditional *Csnk1a1* knockout mouse model in which exon 3 is flanked by loxP sites (*Csnk1a1*$^{fl/fl}$) crossed with Mx1-Cre$^+$ mice, allowing inducible, hematopoietic-specific deletion upon poly(I:C) administration [8]. cKit-enriched bone marrow (BM) cells from *Csnk1a1*$^{fl/fl}$ Mx1-Cre$^+$ (CD45.2$^+$) mice were transduced with retroviral vectors encoding wild-type (WT) *Csnk1a1*, E98V-mutant *Csnk1a1*, or an empty vector (EV), and transplanted into lethally irradiated WT recipients. After hematopoietic reconstitution, poly(I:C) was administered to delete endogenous *Csnk1a1* (Fig. 1A). Consistent with the essential role of CK1α in hematopoiesis, mice receiving EV-transduced cells succumbed to BM failure 53–56 days after transplant (Fig. 1B). In contrast, both WT- and E98V-transduced cells fully rescued hematopoiesis and ensured long-term survival, demonstrating that the E98V mutant retains functional activity in vivo.

Csnk1a1 E98V does not enhance self-renewal or drive clonal expansion

To assess the impact of the *Csnk1a1* E98V mutation on HSC self-renewal, we monitored donor chimerism in primary, secondary and tertiary recipients following bulk transplantation of donor cells (Fig. 1A). WT and E98V groups exhibited comparable reconstitution at all timepoints, with gradual decline in overall engraftment of donor cells across transplants (Fig. 1C). In contrast to the enhanced self-renewal associated with *Csnk1a1* haploinsufficiency [8, 9], the E98V mutation did not confer a competitive advantage or expansion over time, indicating a fundamentally different mechanism of action.

Csnk1a1 E98V remodels the stem cell compartment and alters differentiation trajectories

To determine how *Csnk1a1* E98V affects hematopoiesis without driving clonal expansion, we examined the composition of hematopoietic stem and progenitor cells (HSPCs). Flow cytometric analysis showed an expansion of lin$^-$Sca1$^+$cKit$^+$CD48$^+$CD150$^-$ progenitors (HPC-1) and a trend toward a reduction of lin$^-$Sca1$^+$cKit$^+$CD48$^-$CD150$^-$ multipotent progenitor cells (MPPs) in E98V mice, with these differences becoming more pronounced across successive transplants (Figs. 1D, E, and S1A).

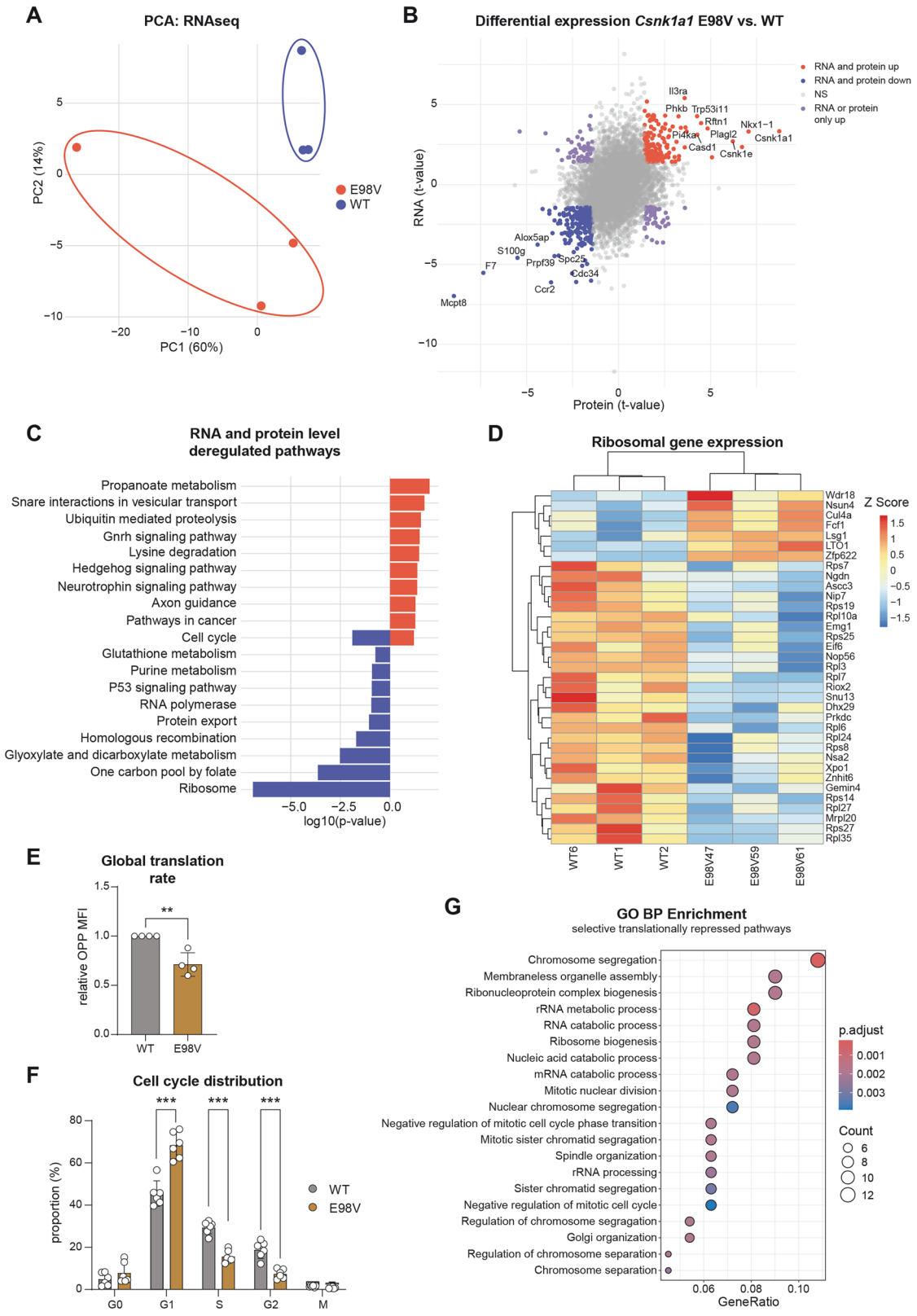
To assess the molecular basis of these compositional changes, we performed bulk RNA-seq of GFP$^+$ lin$^-$Sca1$^+$cKit$^+$ (LSK) cells after the primary transplant. This confirmed transcriptional remodeling of *Csnk1a1* E98V mutant cells compared to the *Csnk1a1* WT control (Fig. S1B, C): cell cycle and DNA replication programs were upregulated, while platelet activation, coagulation, vesicle trafficking, and protein processing pathways were downregulated in *Csnk1a1* E98V mutant cells (Fig. 1F). We next applied CIBERSORTx deconvolution to infer the cellular composition of the bulk RNA samples, using single-cell data from Stalmann et al. as reference data [9] (Fig. 1G and Supplementary Table 3). *Csnk1a1* E98V mice showed minor reductions in LT- and ST-HSCs and a marked reduction in megakaryocyte progenitors. In contrast, MPP2/3 populations were mildly increased, and there was a significant enrichment of lymphoid-biased progenitors. Consistent with these predictions, flow cytometry analysis of secondary transplant bone marrow revealed decreases in CD11b$^+$ myeloid cells and a notable increase in CD19$^+$ B-cells (Fig. S1D), with trends toward lower megakaryocyte progenitors (MkP) and higher common lymphoid progenitors (CLP) (Fig. S1E).

Histological analysis of tibias revealed fewer but larger megakaryocytes in *Csnk1a1* E98V mice compared to controls (Fig. 1H, I), consistent with trends toward lower peripheral blood platelet counts during primary and secondary transplants (Fig. S1F, G). White blood cell, red blood cell, and hemoglobin counts remained unchanged (Fig. S1F, G). Given the established role of CK1α in regulating WNT and p53 signaling, we examined whether Csnk1a1 E98V alters transcriptional programs associated with these pathways. Reactome pathway enrichment analysis revealed enrichment of p53-related gene sets in Csnk1a1 E98V-expressing LSK cells (Fig. 1J), and we observed enrichment of WNT signaling pathways in E98V cell lines (Fig. S1H and Supplementary Table 4). However, these transcriptional changes did not translate to enhanced self-renewal or clonal expansion in serial transplantation assays (Fig. 1C), indicating that canonical WNT and p53 pathway activity alone does not account for the functional consequences of the E98V mutation.

Together, these data indicate that the *Csnk1a1* E98V mutation retains functional activity to sustain hematopoiesis but remodels the HSPC compartment. The mutation biases differentiation toward lymphoid-primed progenitors and impairs megakaryopoiesis, yet does not promote self-renewal or clonal expansion.

The *Csnk1a1* E98V mutation rewires kinase signaling beyond simple loss of function

To dissect the molecular consequences of *Csnk1a1* E98V further, we generated conditionally immortalized hematopoietic progenitor cell lines from *Csnk1a1*$^{fl/fl}$ Mx1-Cre$^+$ and *Csnk1a1*$^{fl/+}$ Mx1-Cre$^+$ bone marrow using the Hoxb8-Flt3L system [14] (Fig. 2A). *Csnk1a1*$^{fl/fl}$ Mx1-Cre$^+$ cells were transduced with retroviral



constructs expressing wild-type (WT) or E98V-mutant *Csnk1a1*, and endogenous *Csnk1a1* was excised through Cre recombination induced by IFNα treatment (Fig. S2A).

The preservation of hematopoietic function with altered differentiation in *Csnk1a1* E98V cells indicated a change-of-function rather than a loss-of-function mutation. As E98 localizes to the kinase domain, we hypothesized that altered catalytic activity and substrate selectivity mediate this phenotype. To test this, we combined kinome activity profiling using the PamGene serine/threonine kinase PamChip microarray with RNA-seq and

Fig. 3 *Csnk1a1* E98V mutation induces coordinated suppression of ribosomal and cell-cycle programs. A PCA of bulk RNA-seq data comparing *Csnk1a1* WT and *Csnk1a1* E98V samples. Individual data points represent one biological replicate. **B** Scatter plot integrating bulk RNA-seq and proteomics differential expression comparing *Csnk1a1* E98V and *Csnk1a1* WT cells. Each point represents RNA and corresponding protein t-values; high or low expression is defined as t-value > ± 1.4. $n = 3$ biological replicates per group. **C** KEGG pathway enrichment analysis of genes deregulated at RNA and protein levels (t-value > ± 1.4, identified in Fig. 3B). Top 10 pathways enriched in up- and down-regulated genes are shown, ranked by -log10(p-value). $n = 3$ biological replicates per group. **D** Heatmap of ribosome-related genes from KEGG database that are represented in bulk RNA-seq data. Expression values are z-score normalized across samples. **E** Global translation rates were assessed by OPP incorporation and flow cytometry analysis. MFI for *Csnk1a1* E98V was normalized to *Csnk1a1* WT samples. Data represent mean ± SD; $n = 4$ independent experiments. Statistical comparisons were performed using a paired two-tailed t test. **F** Cell-cycle distribution was assessed by Ki67 and DAPI staining and flow cytometry analysis. Data represent mean ± SD; $n = 6$ independent experiments. Statistical comparisons were performed using 2-way ANOVA with the Šidák multiple comparisons test. **G** GO BP enrichment analysis of translationally repressed targets ($n = 115$), defined as significantly decreased at the protein level (t-value < −2) but unchanged at the RNA level (| t-value | < 1). Top 20 enriched processes are shown, ranked by gene ratio. Node color indicates adjusted *p*-value, node size reflects gene count per pathway. $n = 3$ biological replicates per group. *$p \le 0.05$; **$p \le 0.01$; ***$p \le 0.001$; ****$p \le 0.0001$. BP biological process, DAPI 4′,6-diamidino-2-phenylindole, GO Gene Ontology, MFI mean fluorescence intensity, OPP O-propargyl-puromycin, PCA principal component analysis, SD standard deviation, WT wild-type.

quantitative phosphoproteomics. These techniques provide complementary information, as PamGene profiling directly measures kinase activity across a panel of peptide substrates, while the untargeted phosphoproteomics captures global phosphorylation at endogenous protein sites.

Kinome activity profiling revealed profound reprogramming of intracellular signaling in *Csnk1a1* E98V-expressing cells. Principal component analysis (PCA) of 71 robustly detected phosphopeptides showed clear separation between WT and E98V samples, whereas *Csnk1a1*$^{-/+}$ haploinsufficient and *Csnk1a1*$^{fl/+}$ control cells clustered closely together, indicating that the E98V variant induces a distinct phosphorylation signature beyond the effects of haploinsufficiency (Fig. S2B, C). Mapping inferred kinase activity onto a kinome tree demonstrated that *Csnk1a1* E98V not only reduced CK1α activity but also caused a near-global suppression of kinase signaling, affecting CMGC, CAMK, and AGC kinase families (Fig. 2B). In contrast, haploinsufficient cells displayed a narrower pattern, with modest CK1α suppression and minor decreases across eight downstream kinases, consistent with proportional dampening of peptide phosphorylation due to reduced gene dosage (Fig. 2C). Phosphosite-level analysis reinforced these differences. *Csnk1a1* E98V cells showed uniformly negative peptide phosphorylation values compared to *Csnk1a1* WT cells, with 48 of 71 peptides (68%) significantly decreased ($p < 0.05$) (Fig. 2D), whereas haploinsufficient cells exhibited more heterogeneous profiles with predominantly downward trends of smaller magnitude. No changes in *Csnk1a1*$^{-/+}$ cells reached statistical significance, indicating only subtle signaling attenuation.

To directly compare phosphorylation profiles between mutation and haploinsufficiency, we systematically analyzed peptide-level changes. While 20 out of the 30 most affected peptides were downregulated in both conditions, each genotype also displayed unique phosphorylation changes (Fig. 2E). *Csnk1a1* E98V cells exhibited selective loss of phosphorylation on peptides such as PLM_76–88 and KPB1_1011–1023, whereas haploinsufficiency uniquely affected sites including GYS2_1–13 and NOS3_1171–1183. The moderate correlation between profiles (Pearson $r = 0.55$) confirmed only partial concordance, which could be explained by altered CK1a substrate specificity in addition to the effects of reduced dosage, although comprehensive biochemical studies will be required to explore these changes in substrate specificity further and confirm the downstream effects on cellular signaling.

Additionally, we assessed steady-state protein phosphorylation levels using mass spectrometry phosphoproteomics. *Csnk1a1* E98V cells showed decreased phosphorylation at 5 of 7 detected known *Csnk1a1* targets, whereas *Csnk1a1*$^{-/+}$ cells displayed a more mixed profile (Fig. 2F). This corroborates the difference in phosphorylation activity seen in the kinome profiling (Fig. 2B, C and Supplementary Table 5). To investigate the biological impact of E98V-linked phosphorylation changes, we performed enrichment analysis of genes containing differentially phosphorylated sites. This highlighted key pathways critical for cell growth and survival, including cell cycle and Notch signaling, as well as cancer-associated pathways (Fig. 2G).

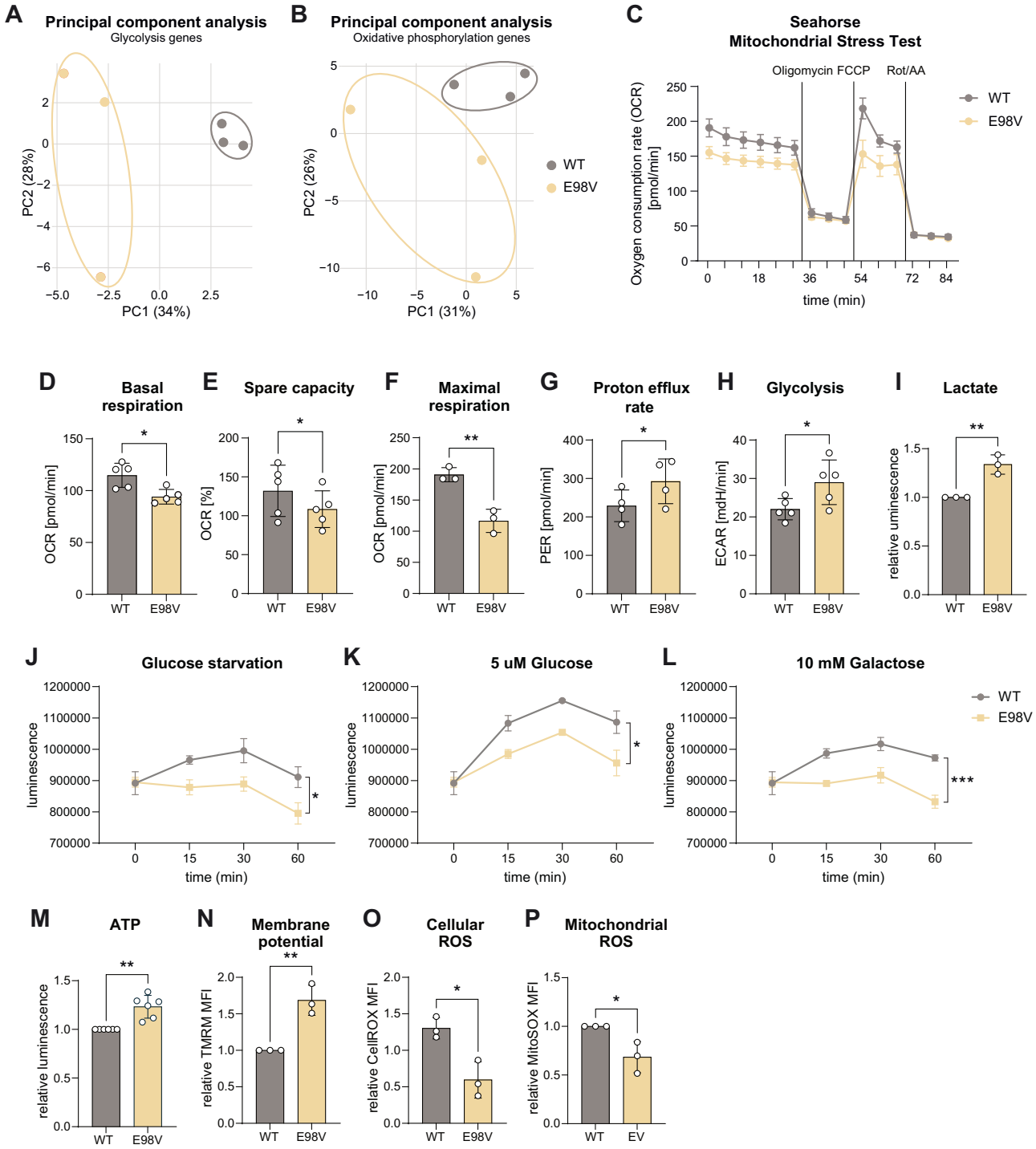
To assess if the deregulated phosphorylation identified in our global phosphoproteomics data parallels the impact on kinase function inferred with the PamGene kinome profiling, we utilized the kinase enrichment tool KEA3 [15]. Since we see global downregulation of phosphorylation predicted according to the peptide signatures, we inferred upstream kinases responsible for the observed phosphorylation changes from the ortholog-mapped list of all gene symbols corresponding to proteins identified to contain phosphosites with decreased phosphorylation (t value < −2) in E98V cells compared to their WT counterparts. This analysis reveals that the top kinases predicted to be upstream of these phosphorylation changes are concordant with those identified by the PamGene profiling, including checkpoint kinases, Aurora kinases A and B, and crucially, CSNK1A1, as well as CSNK2A1 (Fig. 2H). Taken together, the concordance between the PamGene kinome profiling and KEA3 kinase inference strengthens the conclusion that *Csnk1a1* E98V causes broad remodeling of cellular phosphorylation signatures.

Csnk1a1 E98V mutation induces coordinated suppression of ribosomal and cell-cycle programs

To investigate the downstream consequences of altered kinase signaling, we performed transcriptomic and proteomic profiling of *Csnk1a1* WT and *Csnk1a1* E98V cells. Principal component analysis revealed clear separation by genotype across both datasets (Figs. 3A and S3A). Differential expression analysis showed widespread changes, with significant overlap between genes deregulated at the RNA and protein level: 177 were concordantly upregulated and 211 concordantly downregulated in *Csnk1a1* E98V compared to WT cells (Fig. 3B), indicating coordinated changes across transcription and translation. Additionally, we observed considerable overlap between genes deregulated in E98V cell lines and E98V LSK samples: 267 upregulated and 221 downregulated genes based on t-value cutoffs of 1.4 and −1.4, respectively. Pathway analysis of these genes reveals concordant upregulation of cell cycle-linked programs and downregulation of coagulation, additionally highlighting downregulation of many major metabolic pathways that were not among the top downregulated pathways in the LSK cells when analyzed in isolation (Fig. S3B).

KEGG pathway analysis of genes altered by *Csnk1a1* E98V in cell lines at both RNA and protein levels revealed significant suppression of ribosome biogenesis and multiple metabolic pathways, including glutathione and one-carbon metabolism (Fig. 3C). In contrast, upregulated pathways included propanoate metabolism and Hedgehog signaling.

The striking suppression of ribosomal pathways prompted us to examine ribosomal gene expression in more detail. This revealed



widespread downregulation of 28 core ribosomal genes, including Rps14, Rpl27, and Rps7, genes previously implicated in ribosomopathies such as Diamond-Blackfan anemia and del(5q) MDS (Fig. 3D). Conversely, a small group of genes involved in ribosome maturation and rRNA modification was upregulated, suggestive of compensatory activation of ribosome surveillance and assembly pathways.

Ribosomal gene repression was accompanied by significantly reduced global translation rates measured by O-propargyl-puromycin (OPP) incorporation in *Csnk1a1* E98V cells (Fig. 3E). Reduced protein synthesis limits cellular growth capacity. In line with this, cell-cycle profiling revealed accumulation of *Csnk1a1* E98V cells in G1 and reduced proportions in S and G2, corroborating previous observations [8] (Fig. 3F). Beyond this global reduction in translation, we asked whether specific protein classes were selectively affected. We therefore identified 115 proteins significantly decreased at the protein level but unchanged at the RNA level, indicating selective translational repression (Fig. S3C). Pathway analysis of these translationally repressed proteins revealed enrichment for processes related to ribonucleoprotein complex biogenesis, rRNA metabolism, and mitotic progression (Fig. 3G). STRING network analysis further shows two interconnected modules centered on ribosome biogenesis and chromosome segregation (Fig. S3D). These

Fig. 4 The *Csnk1a1* E98V mutation shifts metabolism toward glycolytic dependence. PCA of curated glycolysis (**A**) and oxidative phosphorylation (**B**) gene sets from Gene Ontology database comparing bulk RNA-seq data from *Csnk1a1* WT and *Csnk1a1* E98V samples. Individual data points represent one biological replicate. **C** Representative OCR traces from Seahorse XF mitochondrial stress tests. Oligomycin, FCCP, and Rot/AA were injected sequentially at the indicated time points. Data represent mean ± SD of 8 technical replicates. Quantification of basal respiration (**D**), spare respiratory capacity (**E**), maximal respiration (**F**), proton efflux rate (**G**), and glycolysis (**H**) measured by Seahorse metabolic flux analysis. Data represent mean ± SD. $n = 8$ technical replicates per group from 3 (**F**) or 5 (**D, E, G, H**) independent experiments. Statistical comparisons were performed using paired two-tailed t-tests. **I** Lactate concentration in culture supernatants measured by Lactate-Glo luminescence assay. Luminescence values for *Csnk1a1* E98V were normalized to *Csnk1a1* WT samples. Data represent mean ± SD; $n = 3$ independent experiments. Statistical comparisons were performed using a paired two-tailed t test. Time course measurement of cellular ATP levels during glucose and pyruvate starvation (**J**), followed by reintroduction of glucose (5 mM; **K**) or galactose (10 mM; **L**) for the indicated time points. Data represent mean ± SEM. $n = 3$ independent experiments. Statistical comparisons were performed using 2-way ANOVA with Šidák multiple comparisons test. **M** Cellular ATP levels under basal culture conditions with full nutrient availability. Luminescence values for *Csnk1a1* E98V were normalized to *Csnk1a1* WT samples. Data represent mean ± SD. $n = 6$ independent experiments. Statistical comparisons were performed using paired two-tailed t-tests. **N** Mitochondrial membrane potential measured by TMRM staining and flow cytometry analysis. **O** Cellular ROS measured by CellROX staining and flow cytometry analysis. **P** Mitochondrial ROS measured by MitoSOX staining and flow cytometry analysis. For (**N–P**) MFI for *Csnk1a1* E98V was normalized to *Csnk1a1* WT samples. Data represent mean ± SD. $n = 3$ independent experiments. Statistical comparisons were performed using paired two-tailed t-tests. *$p \le 0.05$; **$p \le 0.01$; ***$p \le 0.001$; ****$p \le 0.0001$. ECAR extracellular acidification rate, FCCP carbonyl cyanide-*p*-trifluoromethoxyphenylhydrazone, MFI mean fluorescence intensity, OCR oxygen consumption rate, PCA principal component analysis, PER proton efflux rate, ROS reactive oxygen species, Rot/AA rotenone/antimycin A, SD standard deviation, SEM standard error of the mean, TMRM tetramethylrhodamine methyl ester, WT wild-type.

transcriptomic, proteomic, and functional data converge to support that *Csnk1a1* E98V cells display coordinated suppression of ribosomal gene transcription and global protein synthesis, with selective translational repression of biosynthetic and cell-cycle programs.

The *Csnk1a1* E98V mutation shifts metabolism toward glycolytic dependence

Given the suppression of kinase signaling, as well as ribosomal and mitotic programs, we next investigated whether the *Csnk1a1* E98V mutation alters cellular metabolism. PCA of curated glycolysis and oxidative phosphorylation (OXPHOS) gene sets revealed clear separation between WT and *Csnk1a1* E98V cells at both transcript and protein levels (Figs. 4A, B and S4A, B), indicating coordinated metabolic reprogramming.

To determine if this transcriptional shift translates to functional metabolic changes, we performed Seahorse metabolic flux analysis. Seahorse analysis revealed a pronounced reduction in mitochondrial respiration in *Csnk1a1* E98V-expressing cells: basal oxygen consumption rate (OCR), spare respiratory capacity, maximal respiration, ATP-linked respiration, and non-mitochondrial respiration were significantly decreased, whereas proton-linked respiration and coupling efficiency remained unchanged (Figs. 4C–F and S4C–F). These findings indicate that while mitochondria remain coupled, they operate at substantially reduced capacity.

Concurrently, glycolytic activity was increased: *Csnk1a1* E98V cells displayed elevated proton efflux rates (PER) and an enhanced extracellular acidification rate (ECAR) following glucose addition compared to WT cells (Fig. 4G, H), accompanied by significantly higher lactate concentrations (Fig. 4I).

To assess whether this metabolic shift affects cellular energetics under stress, we measured intracellular ATP dynamics during substrate deprivation and recovery. Upon glucose and pyruvate starvation, *Csnk1a1* E98V cells exhibited a more pronounced decline in ATP levels compared to WT (Fig. 4J). Glucose reintroduction partially restored ATP production in *Csnk1a1* E98V but remained below WT levels (Fig. 4K).

To test if E98V cells require glycolysis for ATP generation, we replaced glucose with galactose in cell culture media, which forces cells to rely on OXPHOS for ATP production. Under these conditions, the difference between genotypes became even more pronounced. WT cells responded with an ATP increase, reflecting the engagement of OXPHOS, whereas E98V cells failed to compensate, showing a progressive ATP level decline (Fig. 4L), confirming their glycolytic dependence. Despite this metabolic inflexibility, *Csnk1a1* E98V cells maintained elevated steady-state ATP levels under basal conditions with full nutrient availability (Fig. 4M), suggesting compensatory ATP production through enhanced glycolytic flux.

To further characterize mitochondrial dysfunction in *Csnk1a1* E98V cells, we first examined mitochondrial content. mtDNA/nDNA ratios remained unchanged (Fig. S4G), indicating that reduced respiration reflects functional impairment rather than mitochondrial loss. Mitochondrial membrane potential was significantly increased (Fig. 4N). This hyperpolarization, despite reduced respiration, is in line with low mitochondrial ATP production in glycolysis-dependent cells. Consistent with diminished electron flux, both cellular and mitochondrial ROS levels are decreased in *Csnk1a1* E98V cells compared to WT (Fig. 4O, P).

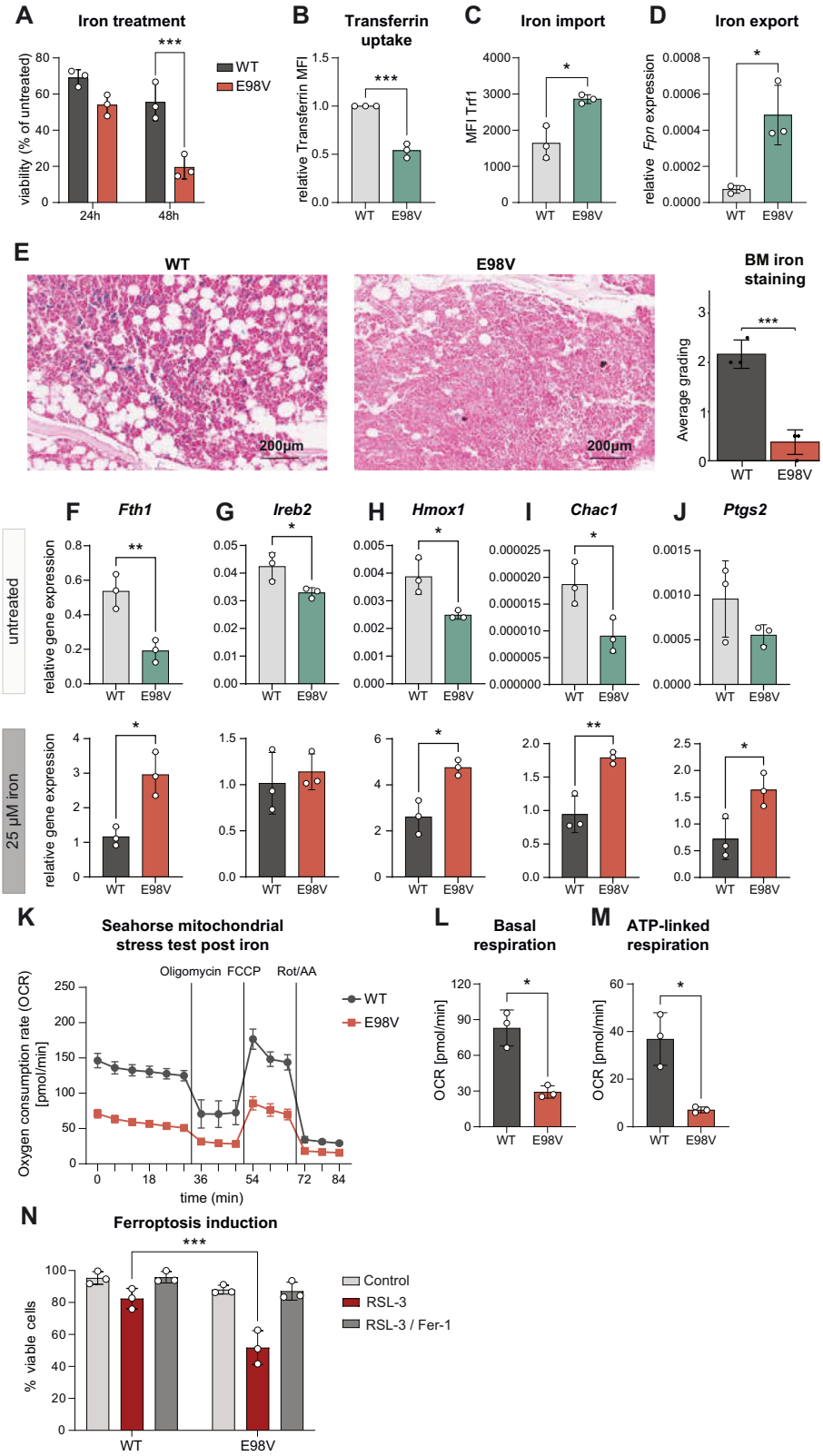
Together, these findings demonstrate that *Csnk1a1* E98V cells shift to glycolytic metabolism due to impaired mitochondrial function, relying predominantly on glycolysis for ATP production with limited capacity to engage OXPHOS under stress.

Csnk1a1 E98V cells display heightened sensitivity to iron and deregulated iron handling

Mitochondrial function depends critically on iron for heme synthesis and iron-sulfur cluster biogenesis. Given the pronounced mitochondrial dysfunction in E98V cells, we investigated whether iron metabolism is also disrupted. *Csnk1a1* E98V-expressing cells exhibited markedly decreased viability in the presence of ammonium iron citrate after 48 h, compared to *Csnk1a1* WT cells (Fig. 5A), indicating heightened sensitivity to iron.

To identify the basis of this vulnerability, we examined iron uptake and homeostasis. Transferrin uptake was impaired in *Csnk1a1* E98V cells (Fig. 5B), despite elevated basal expression of the iron importer Tfr1 and exporter Fpn (Fig. 5C, D), suggesting dysregulated iron trafficking.

To determine whether this deregulated iron handling was reflected in vivo, we assessed stainable iron stores in bone marrow sections from *Csnk1a1* WT and *Csnk1a1* E98V mice (Fig. 1) using Prussian blue staining. *Csnk1a1* E98V bone marrow showed reduced positive staining compared to WT controls, indicating decreased marrow iron stores in vivo. This reduction in stored iron does not contradict the increased iron sensitivity of mutant cells, as Prussian blue detects stored ferric iron rather than labile or poorly buffered intracellular iron pools. Together with impaired transferrin uptake and altered Tfr1/Fpn expression, these findings suggest that *Csnk1a1* E98V disrupts iron compartmentalization and storage rather than simply impacting total iron accumulation.



Transcriptomic analysis revealed that key iron-handling and ferroptosis-related genes, including Fth1, Ireb2, Hmox1, Chac1, and Ptgs2, were downregulated at baseline in E98V cells but strongly induced following iron treatment (Fig. 5E–I), indicating a failure to maintain iron homeostasis and an exaggerated stress response upon iron exposure. To assess the consequences of iron exposure on mitochondrial function, we performed Seahorse mitochondrial stress tests on iron-treated cells. Iron treatment caused a drastic reduction in basal and ATP-linked respiration in mutated cells (Fig. 5J–L), demonstrating that iron overload

Fig. 5 *Csnk1a1* E98V cells display heightened sensitivity to iron and deregulated iron handling. A Cell viability of *Csnk1a1* WT and *Csnk1a1* E98V cells treated with ammonium iron citrate (25 μM) for 24 h and 48 h, measured using the CellTiter-Glo viability assay. Data represent mean ± SD. $n = 3$ independent experiments. Statistical comparisons were performed using 2-way ANOVA with Šidák multiple comparisons test. **B** Transferrin uptake measured by staining with AF647-conjugated transferrin and flow cytometry analysis. MFI for *Csnk1a1* E98V was normalized to *Csnk1a1* WT samples. Data represent mean ± SD. $n = 3$ independent experiments. Statistical comparisons were performed using paired two-tailed t-tests. **C** Basal surface expression of Tfr1 (transferrin receptor 1) measured by flow cytometry. Data represent mean ± SD. $n = 3$ independent experiments. Statistical comparisons were performed using paired two-tailed t-tests. **D** Gene expression of Fpn (ferroportin). Expression was measured by qRT-PCR and normalized to the housekeeping genes Actb and Gapdh. Data represent mean ± SD. $n = 3$ independent experiments. Statistical comparisons were performed using unpaired two-tailed t-tests. **E** Representative images and semi-quantitative assessment of Prussian blue staining in tibial bone marrow sections from *Csnk1a1* WT and *Csnk1a1* E98V mice. Bone marrow iron stores were assessed on Prussian blue-stained femoral bone marrow sections using a simplified semiquantitative scoring system. Iron stores were scored as 0, absent iron; 1, reduced iron; 2, normal iron stores; or 3, increased iron. Scoring was performed blinded to genotype. Data represent mean ± SD. Each point represents one mouse. Statistical comparison was performed using an unpaired two-tailed t-test. **F–J** Gene expression of iron-handling and ferroptosis-related genes at baseline and following treatment with ammonium iron citrate (25 μM) for 24 h. Expression was measured by qRT-PCR and normalized to the housekeeping genes Actb and Gapdh. Data represent mean ± SD. $n = 3$ independent experiments. Statistical comparisons were performed using unpaired two-tailed t-tests. **K** Representative OCR traces from Seahorse XF mitochondrial stress tests. Cells were treated with ammonium iron citrate (25 μM) for 24 h prior to sequential injection of oligomycin, FCCP, and Rot/AA at the indicated timepoints. Data represent mean ± SD of 8 technical replicates. Quantification of basal respiration (**L**) and ATP-linked respiration (**M**) measured by Seahorse metabolic flux analysis following treatment with ammonium iron citrate (25 μM) for 24 h. Data represent mean ± SD. $n = 8$ technical replicates per group from 3 independent experiments. Statistical comparisons were performed using paired two-tailed t-tests. **N** Cell viability of *Csnk1a1* WT and *Csnk1a1* E98V cells treated with RSL-3 (1.13 μM) and Fer-1 (1 μM) for 6 h. Viable cells were quantified by flow cytometry as the percentage of $DAPI^-AnnexinV^-$ populations. Data represent mean ± SD. $n = 3$ biological replicates. Statistical comparisons were performed using 2-way ANOVA with Šidák multiple comparisons test. $^*p \le 0.05$; $^{**}p \le 0.01$; $^{***}p \le 0.001$; $^{****}p \le 0.0001$. AF647, Alexa Fluor 647; Chac1, glutathione-specific gamma-glutamylcyclotransferase 1; Fpn, ferroportin; Fth1, ferritin heavy chain 1; Hmox1, heme oxygenase 1; Ireb2, iron regulatory protein 2; MDS, myelodysplastic neoplasm; MFI, mean fluorescence intensity; OCR, oxygen consumption rate; Ptgs2, prostaglandin-endoperoxide synthase 2 (cyclooxygenase-2); qRT-PCR, quantitative reverse transcription polymerase chain reaction; Rot/AA, rotenone/antimycin A; SD, standard deviation; Tfr1, transferrin receptor 1; WT, wild-type.

severely compromises their already-impaired mitochondrial function. While iron treatment reduced mitochondrial respiration in both genotypes (Fig. S5A), basal respiration showed a significant genotype x treatment interaction (Fig. S5B), indicating a more pronounced effect in *Csnk1a1* E98V cells. In contrast, no significant genotype x treatment interaction was observed for ATP-linked respiration (Fig. S5C). To determine whether the observed iron hypersensitivity reflects susceptibility to ferroptosis, an iron-dependent form of regulated cell death, we treated cells with the ferroptosis inducer RSL-3. *Csnk1a1* E98V cells showed a significantly greater reduction in viability upon RSL-3 treatment compared to WT cells (Fig. 5M). This effect was rescued by co-treatment with the ferroptosis inhibitor Ferrostatin-1, confirming that E98V cells exhibit increased sensitivity to ferroptosis.

Collectively, these data reveal that *Csnk1a1* E98V causes defective iron handling in vivo and in vitro, producing reduced stainable intracellular iron stores but increased vulnerability to iron-induced mitochondrial dysfunction and ferroptosis, a vulnerability that may be therapeutically relevant in del(5q) MDS patients.

CSNK1A1 mutations define a clinically and biologically distinct subgroup of del(5q) MDS

To determine whether the phenotypes observed in *Csnk1a1* E98V experimental models are reflected in human disease, we analyzed clinical parameters in a cohort of 195 del(5q) MDS patients. This cohort included 84 patients harboring *CSNK1A1* mutations (74 with E98 hotspot mutations, 28 with D140 mutations) and 111 patients with WT *CSNK1A1*. The E98-mutant group consisted predominantly of E98K, E98G, E98Q, and E98A variants, whereas E98V mutations were rare in this cohort ($n = 2$) (Supplementary Table 1). As no significant differences were observed between E98- and D140-mutant patients across peripheral blood counts and bone marrow differential parameters (Fig. S6A,C), these variants were analyzed together as a *CSNK1A1*-mutant group for subsequent clinical analyses. Peripheral blood analysis revealed significantly reduced platelet counts in *CSNK1A1*-mutant patients compared to those without *CSNK1A1* mutations (Fig. 6A), consistent with the impaired megakaryopoiesis observed in *Csnk1a1* E98V mice (Fig. 1H, I). White blood cell counts and hemoglobin levels were comparable between groups (Fig. 6B, C). Bone marrow differential analysis showed a significantly increased myeloblast percentage in patients with *CSNK1A1* mutations and elevated eosinophil proportions, while other bone marrow lineage distributions showed no differences (Fig. 6D, E and S6B).

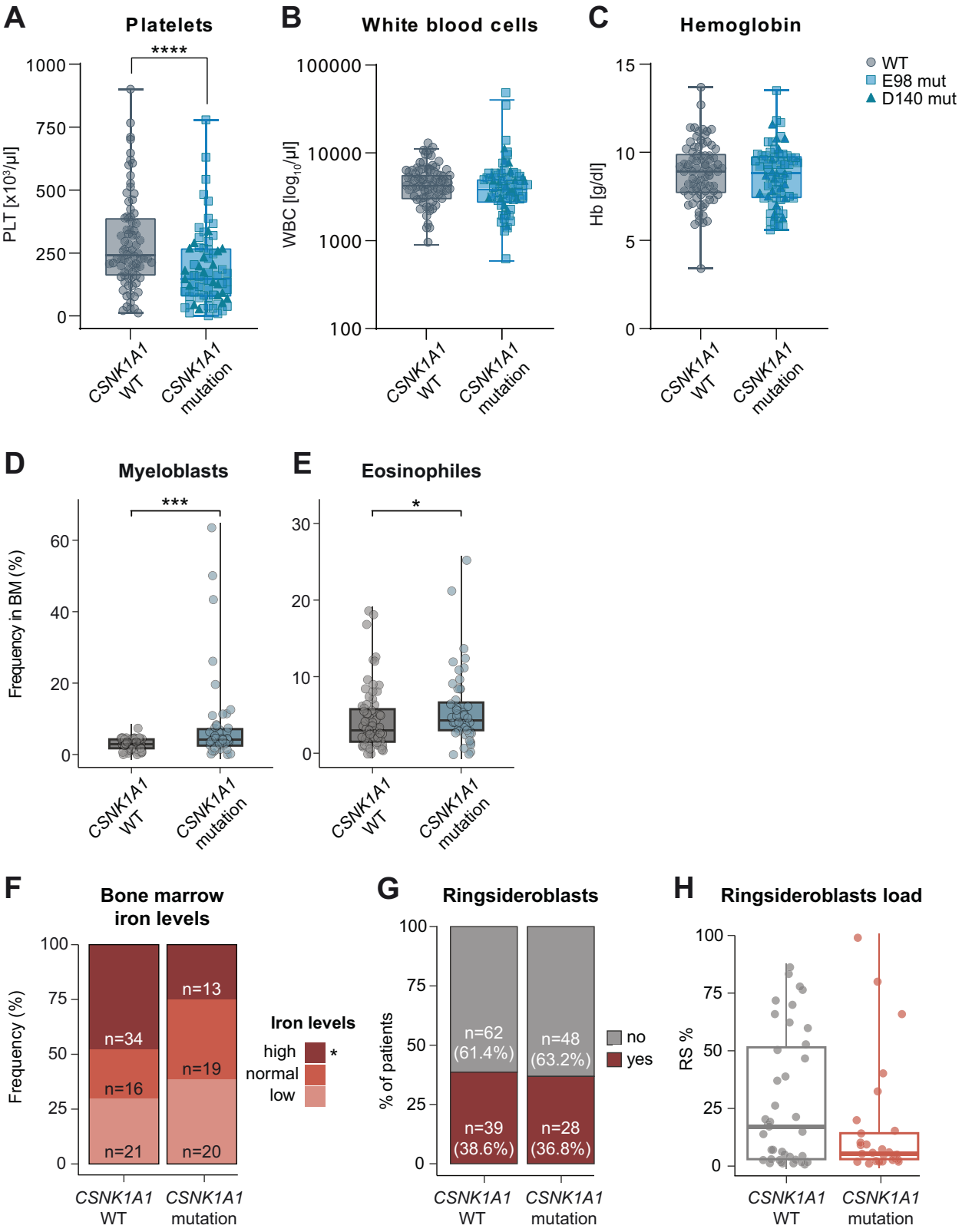
Given the iron sensitivity and reduced stainable marrow iron observed in the *Csnk1a1* E98V model, we examined iron-related parameters in patients. *CSNK1A1*-mutant patients exhibited a lower prevalence of elevated bone marrow iron levels compared to non-mutant del(5q) MDS cases (Fig. 6F). The frequency of patients exhibiting ring sideroblasts was comparable between groups (Fig. 6G), whereas ring sideroblast load showed a trend toward lower levels in CSNK1A1-mutant patients (Fig. 6H). Although transfusion data were not available in this cohort and remain an important confounder, the concordance between the controlled murine model and the human patient cohort supports the possibility that *CSNK1A1* mutations alter marrow iron handling in vivo.

Collectively, these findings indicate that CSNK1A1 mutations define a distinct clinical phenotype in del(5q) MDS, characterized by reduced platelet production, increased myeloblast burden, and features suggestive of altered iron handling. In conjunction with our experimental findings, these observations raise the possibility that dysregulated iron metabolism and ferroptosis sensitivity may represent therapeutic vulnerabilities in this disease subtype.

DISCUSSION

Here, we show that the *Csnk1a1* E98V mutation drives a distinct signaling and metabolic state that reshapes HSC behavior and lineage output, going beyond the proliferative effects of del(5q) haploinsufficiency. Given that *CSNK1A1* mutations recurrently emerge in an already haploinsufficient setting and are associated with poor outcomes, our findings suggest these lesions are not merely additive, but may represent an adaptive shift in cellular regulation.

CK1α is a crucial modulator of multiple cellular processes and a critical regulator of hematopoietic health and disease [16–18]. Our data propose a model in which CK1α functions as a central



signaling hub in HSPCs, whose activity is disrupted by the *Csnk1a1* E98V mutation. Phosphoproteomics and kinome activity profiling revealed widespread downregulation of phosphorylation and kinase activity, which extends beyond canonical CK1α substrates (Fig. 2), reflecting a broad rewiring of signaling networks. These perturbations affect protein translation, cell cycle control, and metabolic signaling, and manifest in vivo as remodeling of the HSPC compartment, including biased lineage output.

At the molecular level, suppression of ribosomal gene expression and global translation mirrors features of ribosomopathies,

Fig. 6 *CSNK1A1* mutations define a clinically and biologically distinct subgroup of del(5q) MDS. Platelet (**A**), WBC (**B**), and hemoglobin (**C**) counts in peripheral blood of patients with del(5q) MDS, including patients with *CSNK1A1* mutations ($n = 80$) and patients without *CSNK1A1* mutations ($n = 71$). Data represent individual patient values on box plots (median, IQR, min-max). Statistical comparison was performed using the Mann-Whitney test with Benjamini-Hochberg correction for multiple testing. **D, E** BM differential counts of patients with del(5q) MDS, including patients with *CSNK1A1* mutations ($n = 80$) and patients without *CSNK1A1* mutations ($n = 104$), are shown as percentages of total nucleated cells. Data represent individual patient values on box plots (median, IQR, min-max). Statistical comparison was performed using the Mann-Whitney test with Benjamini-Hochberg correction for multiple testing. **F** Frequency of low, normal and high BM iron levels in del(5q) MDS, including patients with *CSNK1A1* mutations ($n = 52$) and patients without *CSNK1A1* mutations ($n = 71$). Statistical comparison was performed using the Pearson chi-squared test. **G** Frequency of ring sideroblasts in the BM of patients with del(5q) MDS including patients with *CSNK1A1* mutations ($n = 76$) and patients without *CSNK1A1* mutations ($n = 101$). **H** Ring sideroblast load (%) in the BM of patients with del(5q) MDS including patients with *CSNK1A1* mutations ($n = 76$) and patients without *CSNK1A1* mutations ($n = 101$). Data represent individual patient values on box plots (median, IQR, min-max). *$p \le 0.05$; **$p \le 0.01$; ***$p \le 0.001$; ****$p \le 0.0001$. PLT platelets, Hb hemoglobin, WBC white blood cells, BM bone marrow, RS ring sideroblasts, MDS myelodysplastic neoplasm, IQR interquartile range, WT wild-type.

including Diamond-Blackfan anemia and del(5q) MDS itself, where impaired ribosome biogenesis reshapes lineage commitment, iron handling, and hematopoietic output [19, 20]. While the direct molecular mechanism linking altered CK1α activity to ribosomal gene repression remains to be established, one candidate intermediary is eIF6, a known CK1α substrate, whose phosphorylation at S175 and S235 is required for nuclear export and translational activation of the 60S ribosomal subunit [21]. This provides a plausible route through which altered CK1α substrate specificity in E98V cells could impair ribosome assembly and global translation. Notably, mutations rescuing eIF6-dependent translational defects have been identified in patients with Shwachman-Diamond syndrome, further connecting CK1α-eIF6 signaling to ribosomopathy-like states [22]. Although eIF6 phosphorylation at these sites was not detected in our phosphoproteomic dataset, likely reflecting coverage limitations rather than true absence, this represents a hypothesis warranting direct investigation in future studies. Thus, *Csnk1a1* E98V appears to exacerbate the intrinsic vulnerabilities caused by del(5q)-associated ribosomal haploinsufficiency. Concurrent repression of kinase signaling, translation, and biosynthetic programs could mitigate proteotoxic and metabolic stress, potentially increasing cellular resilience.

Consistent with this, *Csnk1a1* E98V triggers metabolic reprogramming consistent with hematopoietic stress adaptation. Mutant cells exhibit reduced OXPHOS and increased glycolytic activity. In combination with dampened translation and proliferation, this aligns with quiescent HSC programs, where minimizing ROS and anabolic flux supports long-term maintenance [23–25]. This quiescent-like metabolic configuration may favor survival under baseline stress while constraining proliferative expansion, explaining the absence of classical WNT-driven proliferative phenotypes. However, this adaptation imposes marked metabolic inflexibility: when glucose was withdrawn or cells were forced to rely on oxidative phosphorylation, E98V cells failed to sustain ATP levels. Therefore, reprogramming that may be protective at baseline becomes limiting under metabolic challenge, revealing a loss of adaptive capacity.

Hematopoietic lineages with sustained anabolic and translational demands, most notably megakaryocytes, appear particularly sensitive to these constraints. Accordingly, we observe impaired megakaryopoiesis in *Csnk1a1* E98V mutant mice and reduced platelet counts in patients, consistent with recent work identifying CK1α as an essential regulator of thrombopoiesis [26]. This phenotype contrasts with the typical del(5q) MDS picture, in which characteristic hypolobated megakaryocytes in the marrow give rise to normal or elevated platelet counts [27]. In this light, the emergence of thrombocytopenia represents a qualitative shift in disease biology, rather than a simple exaggeration of the canonical del(5q) phenotype.

Beyond lineage-specific defects, *Csnk1a1* E98V cells demonstrate pronounced hypersensitivity to iron-induced stress and ferroptotic cell death. Iron challenge triggered exaggerated induction of iron-handling genes and ferroptosis-associated markers, accompanied by near-complete collapse of mitochondrial respiration. An apparent paradox of our study is that *Csnk1a1* E98V bone marrow showed reduced stainable iron by Prussian blue staining, while mutant cells were hypersensitive to iron exposure. These findings can be reconciled by the fact that Prussian blue detects stored ferric iron, whereas iron toxicity and ferroptosis are driven by labile, poorly buffered iron pools. Thus, reduced Prussian blue staining may reflect impaired iron storage, altered iron compartmentalization, increased iron efflux, or selective loss of iron-loaded mutant cells. This interpretation is supported by impaired transferrin uptake, elevated Tfr1 and Fpn, reduced baseline expression of iron-buffering and ferroptosis-related genes, and exaggerated stress responses upon iron challenge. Consequently, *CSNK1A1*-mutant del(5q) MDS patients showed a trend towards reduced ring sideroblast load, suggesting that mutant cells may be less able to tolerate or sustain mitochondrial iron accumulation. Together, these data suggest that *Csnk1a1* E98V creates a state of iron mismanagement rather than simple iron overload or iron deficiency. The increased sensitivity of *Csnk1a1* E98V cells to RSL-3 and rescue by Ferrostatin-1 further indicate that ferroptosis contributes to this vulnerability. These findings suggest that impaired mitochondrial function and metabolic rigidity render E98V cells unable to tolerate acute oxidative and iron-mediated stress, exposing a noncanonical vulnerability of the seemingly stress-adapted state.

These cellular vulnerabilities are partially reflected in the clinical phenotype. *CSNK1A1* mutations are associated with thrombocytopenia, elevated myeloblast percentages, and a lower prevalence of high serum iron levels, consistent with the lineage bias and altered iron handling observed in our models. Notably, thrombocytopenia in del(5q) MDS has been associated with inferior survival [28], raising the possibility that disruption of CK1α-dependent thrombopoietic programs contributes to the adverse clinical impact of these mutations. Importantly, these findings extend rather than reiterate the original description of CSNK1A1 in del(5q) MDS. Previous studies reported that *Csnk1a1* mutations modulate p53 stability via MDM2-dependent regulation [28] and engage β-catenin–dependent WNT signaling [8]. Transplantation experiments further demonstrated accumulation of mutant HSPCs in G1 phase and a downstream lymphoid bias [8]. In the present study, we confirmed enrichment of WNT- and p53-related transcriptional signatures and observed G1 phase accumulation consistent with these previous reports. Further, we show that E98V is not simply exacerbating loss of CK1α, but induces a mutant-specific adaptive state characterized by broad signaling suppression, reduced translation and cell-cycle activity, metabolic rigidity, impaired megakaryopoiesis, and iron/ferroptosis-associated vulnerability.

Our study defines the intrinsic molecular and cellular consequences of *Csnk1a1* E98V mutations. However, in patients, these mutations arise on a haploinsufficient background of del(5q) genes. Together with microenvironment-derived signals such as stromal

interactions, inflammation, and age-related changes, these factors create cumulative selective pressures that may amplify or dampen E98V-induced cellular programs. Modeling the mutation in isolation enables dissection of causal molecular effects, but future studies will be required to determine whether the stress adaptation we observe confers a selective advantage when acquired as a secondary event to *Csnk1a1* haploinsufficiency. In addition, other recurrent kinase-domain mutations, including alternative E98 and D140 variants, may exert overlapping yet distinct effects, and comparative analyses will be essential to delineate shared versus mutation-specific mechanisms.

In summary, we propose a two-hit model, in which del(5q) haploinsufficiency drives clonal expansion, followed by acquisition of a secondary *CSNK1A1* mutation that enables stress resistance rather than increased proliferation. This adaptive state promotes clonal persistence, while simultaneously exposing liabilities in translation, metabolism, and iron handling that may offer new avenues for del(5q) MDS therapy.

DATA AVAILABILITY

Proteomic and phosphoproteomic data are accessible on PRIDE (accession number PXD074599). Raw RNA sequencing is uploaded to GEO (accession GSE335872); processed data, which can be used to reproduce all analysis, is available on Zenodo (https://doi.org/10.5281/zenodo.19034504).

REFERENCES

1. Arber DA, Orazi A, Hasserjian RP, Borowitz MJ, Calvo KR, Kvasnicka H-M, et al. International consensus classification of myeloid neoplasms and acute leukemias: integrating morphologic, clinical, and genomic data. Blood. 2022;140:1200–28.
2. Khoury JD, Solary E, Abla O, Akkari Y, Alaggio R, Apperley JF, et al. The 5th edition of the World Health Organization classification of haematolymphoid tumours: myeloid and histiocytic/dendritic neoplasms. Leukemia. 2022;36:1703–19.
3. Haase D, Germing U, Schanz J, Pfeilstöcker M, Nösslinger T, Hildebrandt B, et al. New insights into the prognostic impact of the karyotype in MDS and correlation with subtypes: evidence from a core dataset of 2124 patients. Blood. 2007;110:4385–95.
4. Ebert BL. Molecular dissection of the 5q deletion in myelodysplastic syndrome. Semin Oncol. 2011;38:621–6.
5. Liu C, Li Y, Semenov M, Han C, Baeg G-H, Tan Y, et al. Control of β-catenin phosphorylation/degradation by a dual-kinase mechanism. Cell. 2002;108:837–47.
6. Elyada E, Pribluda A, Goldstein RE, Morgenstern Y, Brachya G, Cojocaru G, et al. CKIα ablation highlights a critical role for p53 in invasiveness control. Nature. 2011;470:409–13.
7. Bidère N, Ngo VN, Lee J, Collins C, Zheng L, Wan F, et al. Casein kinase 1α governs antigen-receptor-induced NF-κB activation and human lymphoma cell survival. Nature. 2009;458:92–96.
8. Schneider RK, Ademà V, Heckl D, Järås M, Mallo M, Lord AM, et al. Role of casein kinase 1A1 in the biology and targeted therapy of del(5q) MDS. Cancer Cell. 2014;26:509–20.
9. Stalmann USA, Ticconi F, Snoeren IAM, Li R, Gleitz HFE, Cowley GS, et al. Genetic barcoding systematically compares genes in del(5q) MDS and reveals a central role for CSNK1A1 in clonal expansion. Blood Adv. 2022;6:1780–96.
10. Krönke J, Fink EC, Hollenbach PW, MacBeth KJ, Hurst SN, Udeshi ND, et al. Lenalidomide induces ubiquitination and degradation of CK1α in del(5q) MDS. Nature. 2015;523:183–8.
11. Bello E, Pellagatti A, Shaw J, Mecucci C, Kušec R, Killick S, et al. CSNK1A1 mutations and gene expression analysis in myelodysplastic syndromes with del(5q). Br J Haematol. 2015;171:210–4.
12. Heuser M, Meggendorfer M, Cruz MMA, Fabisch J, Klesse S, Köhler L, et al. Frequency and prognostic impact of casein kinase 1A1 mutations in MDS patients with deletion of chromosome 5q. Leukemia. 2015;29:1942–5.
13. Smith AE, Kulasekararaj AG, Jiang J, Mian S, Mohamedali A, Gaken J, et al. CSNK1A1 mutations and isolated del(5q) abnormality in myelodysplastic syndrome: a retrospective mutational analysis. Lancet Haematol. 2015;2:e212–221.
14. Redecke V, Wu R, Zhou J, Finkelstein D, Chaturvedi V, High AA, et al. Hematopoietic progenitor cell lines with myeloid and lymphoid potential. Nat Methods. 2013;10:795–803.
15. Kuleshov MV, Xie Z, London ABK, Yang J, Evangelista JE, Lachmann A, et al. KEA3: improved kinase enrichment analysis via data integration. Nucleic Acids Res. 2021;49:W304–W316.
16. Jiang S, Zhang M, Sun J, Yang X. Casein kinase 1α: biological mechanisms and theranostic potential. Cell Commun Signal. 2018;16:23.
17. Knippschild U, Wolff S, Giamas G, Brockschmidt C, Wittau M, Würl PU, et al. The role of the casein kinase 1 (CK1) family in different signaling pathways linked to cancer development. Onkologie. 2005;28:508–14.
18. Cheong JK, Virshup DM. Casein kinase 1: Complexity in the family. Int J Biochem Cell Biol. 2011;43:465–9.
19. Ebert BL, Pretz J, Bosco J, Chang CY, Tamayo P, Galili N, et al. Identification of RPS14 as a 5q- syndrome gene by RNA interference screen. Nature. 2008;451:335–9.
20. Khajuria RK, Munschauer M, Ulirsch JC, Fiorini C, Ludwig LS, McFarland SK, et al. Ribosome levels selectively regulate translation and lineage commitment in human hematopoiesis. Cell. 2018;173:90–103. e19.
21. Guo J, Jin Z, Yang X, Li J-F, Chen J-G. Eukaryotic initiation factor 6, an evolutionarily conserved regulator of ribosome biogenesis and protein translation. Plant Signal Behav. 2011;6:766–71.
22. Kennedy AL, Myers KC, Bowman J, Gibson CJ, Camarda ND, Furutani E, et al. Distinct genetic pathways define pre-malignant versus compensatory clonal hematopoiesis in Shwachman-Diamond syndrome. Nat Commun. 2021;12:1334.
23. Simsek T, Kocabas F, Zheng J, DeBerardinis RJ, Mahmoud AI, Olson EN, et al. The distinct metabolic profile of hematopoietic stem cells reflects their location in a hypoxic niche. Cell Stem Cell. 2010;7:380–90.
24. Ito K, Carracedo A, Weiss D, Arai F, Ala U, Avigan DE, et al. A PML–PPAR-δ pathway for fatty acid oxidation regulates hematopoietic stem cell maintenance. Nat Med. 2012;18:1350–8.
25. Takubo K, Nagamatsu G, Kobayashi CI, Nakamura-Ishizu A, Kobayashi H, Ikeda E, et al. Regulation of glycolysis by PDK functions as a metabolic checkpoint for cell cycle quiescence in hematopoietic stem cells. Cell Stem Cell. 2013;12:49–61.
26. Kollotzek F, Mott K, Fischer M, Findik B, Göb V, Manke M-C, et al. Casein kinase 1α essentially regulates thrombopoiesis by driving megakaryocyte maturation and cytoskeleton organization. Blood. 2025;146:1964–78.
27. Sokal G, Michaux J, Van Den Berghe H, Cordier A, Rodhain J, Ferrant A, et al. A new hematologic syndrome with a distinct karyotype: the 5 q– chromosome. Blood. 1975;46:519–33.
28. Jonasova A, Cermak J, Vondrakova J, Siskova M, Hochova I, Kadlckova E, et al. Thrombocytopenia at diagnosis an important negative prognostic marker in isolated 5q− MDS (IPSS low and intermediate-1). Leuk Res. 2012;36:e222–e224.

ACKNOWLEDGEMENTS

The authors thank all members of the Schneider laboratory in the Department of Developmental Biology, Erasmus MC, Netherlands, and the INTERCEPT-MDS Innovative Training Network for scientific discussions, and the staff of the Erasmus Laboratory Animal Science Center (EDC) facility at Erasmus MC for their help with experiments.

AUTHOR CONTRIBUTIONS

SS designed and carried out experiments, analyzed results, and wrote the manuscript; JEP designed experiments, performed bioinformatic analysis, and wrote the manuscript; SMH designed and carried out experiments, analyzed results; GVW, IAMS, USAS, SNRF and CM performed experiments; AJFD and JS-R advised on bioinformatic analysis; GF and JO performed mass spectrometry and data preprocessing; EMB performed RNA-sequencing and data preprocessing; WW and TH provided patient data and scientific input; EVV performed and analyzed kinase activity profiling; OC, FS and AL provided important conceptual advice; HFEG performed experiments, supervised the study, and wrote the manuscript; RKS obtained funding, designed and supervised the study, and wrote the manuscript.

FUNDING

RKS is an Oncode Institute investigator and is supported by the European Research Council (Rewind-MF ERC-CoG 101124542; deFIBER ERC-StG 757339; ERC PoC DeAlarmin), a ZonMw VIDI grant (09150172110021), and a KWF Kankerbestrijding Young Investigator Grant (11031/2017-1, Bas Mulder Award; Dutch Cancer Foundation). RKS served as PI of the INTERCEPT-MDS Innovative Training Network, in which SS was supported as a PhD student, funded by the European Union's Horizon 2020 research and innovation programme under the Marie Skłodowska-Curie grant agreement no. 953407. This work was further supported by the Stiftung Deutsche José Carreras Leukämie-Stiftung to FS and RKS (DJCLS 01 R/2021; 2021-20250), and by grants from the Deutsche Forschungsgemeinschaft (DFG; German Research Foundation) to HG (417911533) and RKS (504777725, 417911533, 514007497). This work was also supported by the Corona Foundation (S199/10084/

2021), the Deutsche Forschungsgemeinschaft to E.P.C.v.d.V. (SFB TRR219, Project-ID 322900939, subproject M07; INST 222/1598-1 FUGG, Project 566187929), and the "Netzwerke 2021" programme of the Ministry of Culture and Science of the State of North Rhine-Westphalia through the CANTAR network. Additional support was provided by the Instituto de Salud Carlos III, Ministerio de Economía y Competitividad, Spain (PI23/00007, co-funded by the European Regional Development Fund; PMP24/00025), Generalitat de Catalunya (2021 SGR 00560), the CERCA Programme/Generalitat de Catalunya, and the Fundació Internacional Josep Carreras. HFEG is supported by a ZonMW VENI grant and an Erasmus Medical Center Fellowship. Open Access funding enabled and organized by Projekt DEAL.

COMPETING INTERESTS

JSR reports in the last 3 years funding from GSK and Pfizer & fees/honoraria from Travere Therapeutics, Stadapharm, Astex Pharmaceuticals, Owkin, Pfizer, Vera Therapeutics, Grunenthal, Tempus, and Moderna. AD reports in the last 3 years fees/honoraria from Tempus and MONTAI. RKS is a co-founder and shareholder of Sequantrix GmbH and receives research funding from Active Biotech.

ADDITIONAL INFORMATION

Supplementary information The online version contains supplementary material available at https://doi.org/10.1038/s41375-026-03122-x.

Correspondence and requests for materials should be addressed to Rebekka K. Schneider.

Reprints and permission information is available at http://www.nature.com/reprints

Publisher's note Springer Nature remains neutral with regard to jurisdictional claims in published maps and institutional affiliations.

Open Access This article is licensed under a Creative Commons Attribution 4.0 International License, which permits use, sharing, adaptation, distribution and reproduction in any medium or format, as long as you give appropriate credit to the original author(s) and the source, provide a link to the Creative Commons licence, and indicate if changes were made. The images or other third party material in this article are included in the article's Creative Commons licence, unless indicated otherwise in a credit line to the material. If material is not included in the article's Creative Commons licence and your intended use is not permitted by statutory regulation or exceeds the permitted use, you will need to obtain permission directly from the copyright holder. To view a copy of this licence, visit http://creativecommons.org/licenses/by/4.0/.

© The Author(s) 2026